

Adiabatic quantum state transfer in a semiconductor quantum-dot spin chain

Yadav P. Kandel,¹ Haifeng Qiao,¹ Saeed Fallahi,^{2,3} Geoffrey C. Gardner,^{3,4} Michael J. Manfra,^{2,3,4,5} and John M. Nichol^{1,*}

¹*Department of Physics and Astronomy, University of Rochester, Rochester, NY, 14627 USA*

²*Department of Physics and Astronomy, Purdue University, West Lafayette, IN, 47907 USA*

³*Birck Nanotechnology Center, Purdue University, West Lafayette, IN, 47907 USA*

⁴*School of Materials Engineering, Purdue University, West Lafayette, IN, 47907 USA*

⁵*School of Electrical and Computer Engineering,
Purdue University, West Lafayette, IN, 47907 USA*

Semiconductor quantum-dot spin qubits are a promising platform for quantum computation, because they are scalable and possess long coherence times. In order to realize this full potential, however, high-fidelity information transfer mechanisms are required for quantum error correction and efficient algorithms. In this work, we demonstrate adiabatic quantum-state transfer in a chain of semiconductor quantum-dot spin qubits. By adiabatically modifying the inter-qubit couplings, we transfer single- and two-qubit states between distant electrons. We also show that this method can be cascaded for quantum-state transfer in long qubit arrays. Adiabatic quantum-state transfer is robust to noise and pulse-timing errors. This method will be useful for initialization, state distribution, and readout in large spin-qubit arrays for gate-based quantum computing. It also opens up the possibility of universal adiabatic quantum computing in semiconductor quantum-dot spin qubits.

I. INTRODUCTION

Progress towards fabrication of large spin-qubit arrays [1, 2], together with methods for orthogonal control of quantum-dot chemical potentials [2–4], inter-dot tunnel couplings [5–9], and nearest neighbor exchange couplings [10], have opened up the possibilities of implementing complex multi-qubit quantum operations [11, 12] in semiconductor quantum-dot spin qubits. To tap the full potential of these developments, and to realize a large scale fault-tolerant quantum computer, high-fidelity information transfer mechanisms between qubits are required. Since quantum-dot spin qubits naturally interact through the nearest-neighbor Heisenberg exchange coupling, long distance inter-qubit coupling is challenging. Quantum information transfer has been achieved in spin-qubits by electron shuttling using electrical pulses [3, 13–15], mechanical waves [16], spin SWAP operations [11, 17], and quantum mediators [18, 19]. These methods, elegant as they are, have their limitations, often including stringent pulse-timing requirements. In this work, we report evidence for the successful experimental implementation of adiabatic evolution methods to achieve quantum information transfer in a spin-qubit quantum processor. Compared to conventional pulsed information transfer methods, adiabatic techniques are more robust to pulse errors and system noise.

Adiabatic quantum information processing in arrays of spin qubits has been the focus of intense theoretical research [20–28], due to the possibility of high-fidelity operations in the presence of noise or pulse errors. Adi-

abatic shuttling of spin states has been already demonstrated via electron shuttling [3, 13–15]. Here, we present evidence for adiabatic quantum-state transfer (AQT) of both single-spin eigensates and two-spin entangled states in a GaAs quadruple quantum-dot device. Unlike previous works, this approach does not involve the physical motion of electrons. Specifically, we design a time-dependent Hamiltonian for a system of three qubits. As the qubits evolve under the action of the Hamiltonian, an initial state of the first qubit is transferred to the third qubit. This process is closely related to stimulated adiabatic Raman passage, a time-honored technique from the optical physics community [29], which has been implemented in other qubit platforms [29–32]. Also, the process we use is identical to adiabatic quantum teleportation [21, 23].

We simulate our experiment, taking into account known sources of errors and noise [33], and we find that the results of our simulations closely match the experimental data. In lieu of full quantum-state tomography, which would require a micromagnet [34] or an antenna [35] for magnetic resonance, we implement different quantum gates to assess the qubit states after AQT. The main limiting factor of the AQT fidelity in our experiment is the nuclear hyperfine noise in the GaAs/AlGaAs heterostructure. In the future, we expect AQT to perform better in Si spin qubits, which feature significantly lower hyperfine noise than GaAs devices. In Si devices, we expect that high-fidelity transfer of arbitrary single-qubit states could easily be achieved [23, 33].

II. DEVICE

Our quadruple-quantum-dot device with overlapping gates is fabricated in a GaAs/AlGaAs heterostructure

* john.nichol@rochester.edu

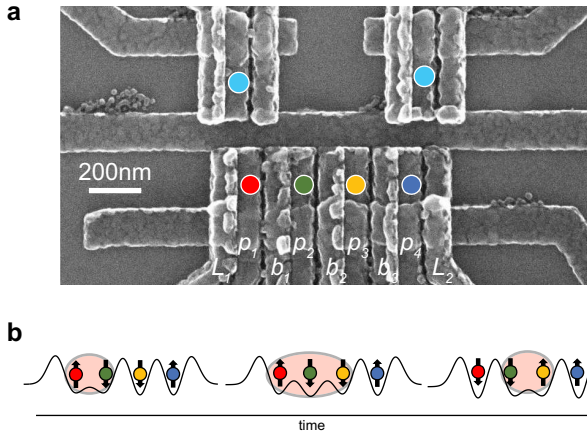


FIG. 1. Experimental setup. (a) Scanning electron micrograph of a quadruple quantum dot device similar to the one used in the experiment. The quantum-dots are located in the two-dimensional electron gas in a GaAs/AlGaAs heterostructure below the positions marked by circles. (b) Schematic showing the changes in the quantum-dot barrier heights for an AQT process that transfers the state of qubit 3 to qubit 1. This process also transfers the entangled state of qubits 1-2 to 2-3.

[Fig. 1(a)] [1, 36]. Two additional dots above the main array are configured for readout via rf-reflectometry [37]. We divide the quadruple quantum dot array into two pairs for initialization and measurement. Dots 1 and 2 form the “left” side and dots 3 and 4 form the “right” side. We measure the left and right pairs in the two-electron singlet/triplet basis using Pauli spin blockade together with a shelving mechanism [38]. The singlet is $|S\rangle = \frac{1}{\sqrt{2}}(|\uparrow\downarrow\rangle - |\downarrow\uparrow\rangle)$, and the triplets are $|T^0\rangle = \frac{1}{\sqrt{2}}(|\uparrow\uparrow\rangle + |\downarrow\downarrow\rangle)$, $|T^+\rangle = |\uparrow\uparrow\rangle$, and $|T^-\rangle = |\downarrow\downarrow\rangle$. The device is operated at the symmetric tuning [39, 40], where each dot contains one electron, and all chemical potentials are roughly the same. We independently control the exchange couplings between dots using the techniques described in Ref. [10].

The time-dependent Hamiltonian of the four-qubit system is

$$H(t) = \frac{\hbar}{4} \sum_{i=1}^3 J_i(t) \boldsymbol{\sigma}_i \cdot \boldsymbol{\sigma}_{i+1} + \frac{\hbar}{2} \sum_{i=1}^4 B_i^z \sigma_i^z, \quad (1)$$

where $J_i(t)$ is nearest-neighbor exchange interaction between spins in quantum dots i and $i+1$ at time t , and B_i^z is the z -component of the magnetic field at the location of dot i . Both J_i and B_i^z have units of frequency. $\boldsymbol{\sigma}_i = [\sigma_i^x, \sigma_i^y, \sigma_i^z]$ is the Pauli vector operating on spin i , and \hbar is the Planck constant. B_i^z accounts for both the external field of 0.5 T applied to polarize the spin states and the local hyperfine field [33].

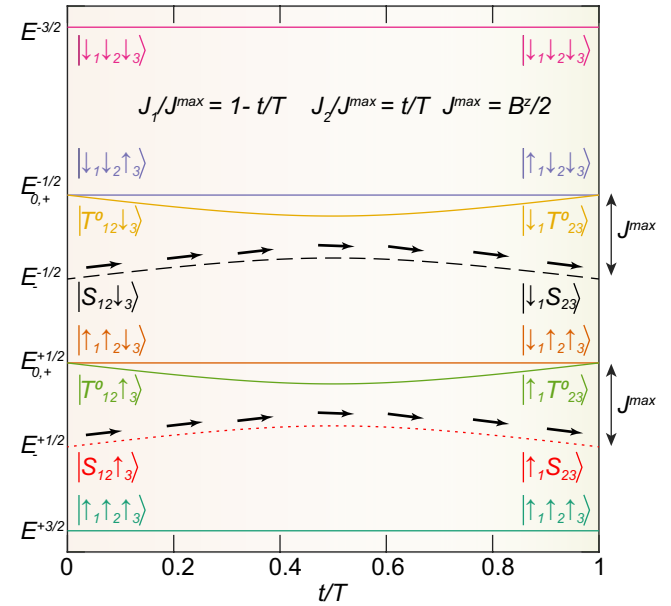


FIG. 2. Eigenstates of the time-dependent three-spin Heisenberg Hamiltonian with $[J_1(t), J_2(t)] = J^{max}[1-t/T, t/T]$ for $0 < t < T$. B^z is the uniform magnetic field. The eigenstates at the initial and final times are labeled. Adiabatic state transfer can occur by initializing the system in either the $E_-^{1/2}$ or $E_-^{-1/2}$ states. Here, the superscript is z -component of the spin angular momentum (S^z), and subscripts denote different eigenstates within a particular S^z subspace.

III. ADIABATIC QUANTUM-STATE TRANSFER

To demonstrate adiabatic spin-state transfer, we initialize the qubit chain in the state $|S_{12} \downarrow 3 \uparrow\rangle$ or $|S_{12} \uparrow 3 \downarrow\rangle$. Dots 3 and 4 contain spins in the $|\downarrow 3 \uparrow\rangle$ or $|\uparrow 3 \downarrow\rangle$ configuration depending on the sign of the hyperfine gradient associated with dots 3 and 4 [41, 42]. We set $[J_1(t), J_2(t), J_3(t)] = J^{max}[1-t/T, t/T, 0]$ for $0 < t < T$, with $J^{max} = 120$ MHz. Note that the initial state discussed above is an eigenstate of $H(0)$ when $J_1(0) \gg |B_2^z - B_1^z|$. Figure 2 shows the time-dependent eigenvalues of the three-spin analog of this Hamiltonian for a related configuration of exchange couplings. Because the total angular momentum and the z -component of angular momentum, S^z , both are conserved in Eq. 1, the four-qubit state remains in the same eigenstate during adiabatic evolution. In particular, an initial state of qubits 1-3, $|S_{12} \downarrow 3\rangle$, transitions to $|\downarrow_1 S_{23}\rangle$, as shown in Fig. 2. Likewise, $|S_{12} \uparrow 3\rangle$ transitions to $|\uparrow_1 S_{23}\rangle$. Figure 1(b) illustrates the physical implementation of this AQT process.

To measure the spin states after the AQT process, we apply SWAP operations [11] between qubits 3-4 and 2-3, in this order, to bring the entangled state to the right pair and the product state to the left pair of spin qubits before measurement [Fig. 3(a)]. We measure the left pair by adiabatic projection and the right pair by diabatic

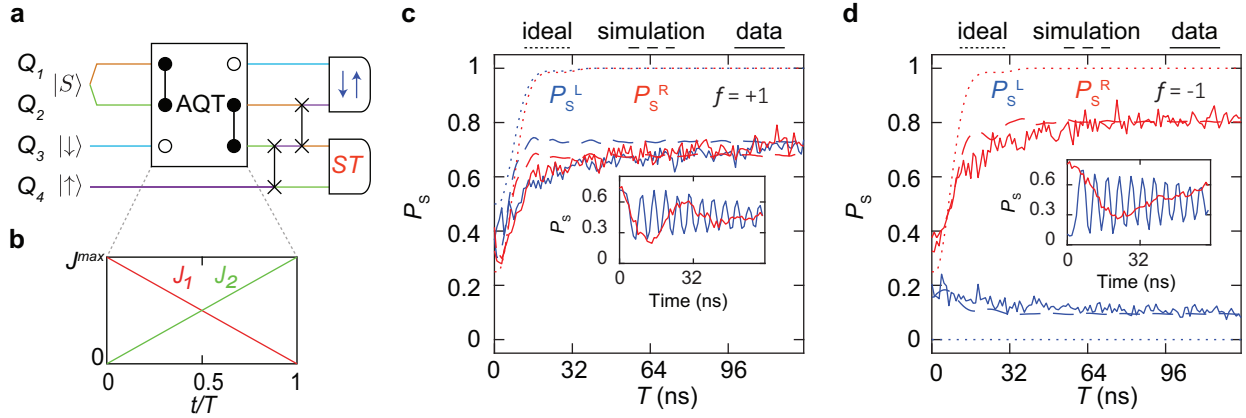


FIG. 3. Three-spin AQT. (a) Quantum circuit diagram for the experiment. The qubit chain is initialized as $|S_{12}\downarrow_3\uparrow_4\rangle$ and the AQT implemented in qubits 1-3 transfers the spin state of qubit 3 to qubit 1 and the entangled state in qubits 1-2 to qubits 2-3. Then, qubits 3-4 and 2-3 are swapped, in this order. We then measure the left pair (P_S^L) and the right pair (P_S^R) in the singlet/triplet basis via Pauli spin blockade. The colors represent the physical locations of the initial states. (b) Change in exchange coupling strengths between qubits for the AQT step in (a). (c) Singlet return probabilities of the left and right pairs as a function of interpolation time T for $f = +1$. (d) Same as (c), but for $f = -1$. In both (c) and (d), the expected outcomes under ideal conditions (dotted lines) as well as simulated results including known errors and noise (dashed lines) are overlaid on top of the measured data (solid lines). The insets in (c) and (d) show exchange oscillations in qubits 1-2 and $S - T^0$ oscillation in qubits 3-4 after the experiment described in (a). The presence of exchange oscillations in qubits 1-2 and $S - T^0$ oscillations in qubits 3-4 confirms successful adiabatic transfer. Each data point represents the average of 512 single-shot measurements.

projection onto the singlet/triplet basis [41, 42]. Diabatic projection preserves the singlet state, and adiabatic projection maps either $|\uparrow\downarrow\rangle$ or $|\downarrow\uparrow\rangle$ to the singlet, and all other states to the triplets, depending on the sign of the hyperfine gradient [33, 41, 42].

Since the initial product state of the left pair is eventually measured in the right pair, knowledge of the magnetic-field gradients in both pairs is required for proper interpretation of the experimental data. We define $f = \text{sign}(B_2^z - B_1^z) \times \text{sign}(B_4^z - B_3^z)$. When $f = +1$, both pairs have gradients of the same sign, and when $f = -1$, the pairs have gradients with opposite signs. To measure f , we initialize both sides as product states with $S^z = 0$. Then, we evolve qubits 2-3 under exchange coupling for variable amount of time. When $f = +1$, corresponding to initial states $|\uparrow_1\downarrow_2\uparrow_3\downarrow_4\rangle$ or $|\downarrow_1\uparrow_2\downarrow_3\uparrow_4\rangle$, prominent exchange oscillations are visible. When $f = -1$, corresponding to initial states $|\downarrow_1\uparrow_2\uparrow_3\downarrow_4\rangle$ or $|\uparrow_1\downarrow_2\downarrow_3\uparrow_4\rangle$, spins 2 and 3 have the same orientation, and no exchange oscillations occur. We interleaved these measurements of f with measurements of the AQT process to distinguish the $f = \pm 1$ cases.

Figures 3(c)-(d) show the results of the experiment described by the circuit of Fig. 3(a) for the $f = +1$ and $f = -1$ cases, respectively. Calculated outcomes for the ideal cases, and simulation results taking into account all known sources of noise and errors, are overlaid on top of the data. The simulation results match the measurements in both cases [33]. In Figs. 3(c)-(d), the gradual rise in the return probability with T occurs because for small values of T , the process is not sufficiently adiabatic. At large values of T , the return probabilities saturate, suggesting successful adiabatic transfer. The predicted

oscillations in the return probability at small values of T are related to resonant adiabatic transfer, which we discuss further below.

Each data point in Fig. 3 is averaged over 512 single-shot measurements for each value of T . We repeat this sequence of 512 single-shot measurements 256 different times. Each repetition takes no more than one second to acquire, and the hyperfine gradients and the value of f are empirically quasi-static during each repetition. Different repetitions were thus used for the $f = +1$ and $f = -1$ cases shown in Fig. 3. The full dataset, which includes all repetitions, is shown in the supplementary material [33]. We display single repetitions here, because the approximately constant value of the hyperfine field during a single repetition enables accurate simulation.

To verify the success of the AQT, we use additional quantum gates to test the qubit states. First we transfer the qubit states as described above with $J^{max} = 120$ MHz and $T = 127$ ns. Then, we perform the SWAP gates discussed previously. In the case of successful state transfer, the initial product state of qubits 3-4 occupies qubits 1-2, and the initial entangled state of qubits 1-2 occupies qubits 3-4. Then, we induce exchange coupling between qubits 1 and 2 for a variable amount of time. If and only if qubits 1 and 2 are in a product state with $S^z = 0$, as expected, exchange oscillations will occur. We also allow qubits 3-4 to evolve for a variable length of time while separated. Clear singlet-triplet oscillations will occur if and only if qubits 3-4 are entangled with $S^z = 0$. The results of these experiments are shown in the insets of Figs. 3(c)-(d) [33]. The presence of coherent oscillations on both sides proves successful transfer

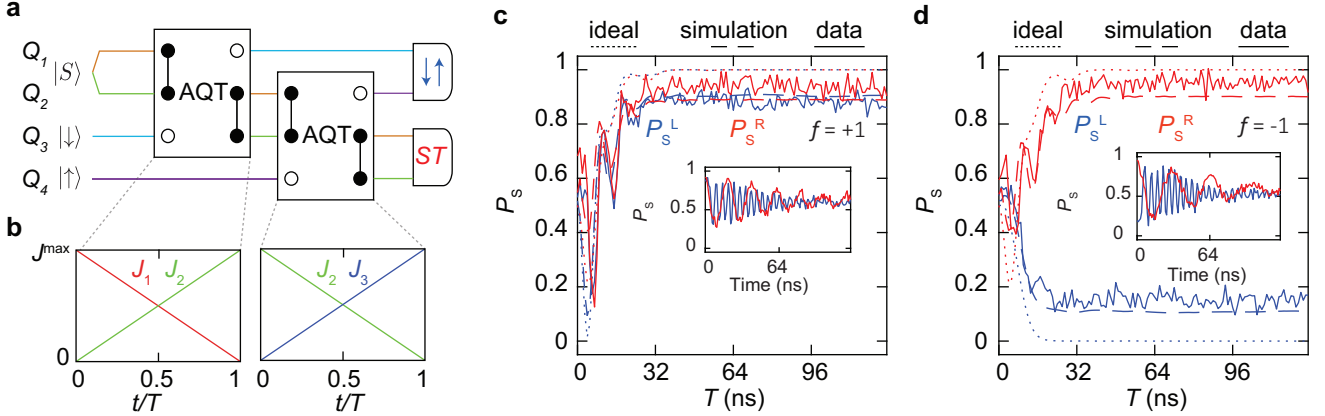


FIG. 4. AQT Cascade. (a) Quantum circuit diagram for the experiment. We initialize the qubits as $|S_{12} \downarrow_3 \uparrow_4\rangle$. Applying two AQT steps transfers the product state of qubits 3-4 to 1-2, and the entangled state of qubits 1-2 to qubits 3-4. (b) Exchange coupling parameters as a function of time for the AQT steps shown in (a). (c) Singlet return probabilities for the left pair (P_S^L) and the right pair (P_S^R) when $f = +1$. (d) Data for $f = -1$. Simulations neglecting and including known sources of error are overlaid in each panel. The insets in (c) and (d) show prominent exchange oscillations between qubits 1-2 and singlet-triplet oscillations associated with qubits 3-4, after the AQT cascade described in (a), confirming successful transfer of qubit states. Each data point represents the average of 256 single-shot measurements.

of both spin-up and spin-down eigenstates from qubit 3 to 1 and an entangled state from qubits 1-2 to 2-3 during the AQT process. The exchange oscillations of qubits 1-2 have different phases for $f = \pm 1$, as expected.

The AQT sequence described above resembles the “counterintuitive” adiabatic transfer sequence used in optical systems [23, 29]. The sequence of Fig. 3(a) transfers a spin state from dot 3 to dot 1, yet the sequence begins with a strong exchange coupling between dots 1 and 2, neither of which contain the state to be transferred. It is also possible to implement a true counterintuitive transfer in our case by starting with all exchange couplings set to zero [33].

Although our AQT process begins with two of the three qubits in a singlet state, these two can in principle be configured in any eigenstate of the exchange operator. However, as Fig. 2 shows, many of the configurations involving other eigenstates of exchange pass through degeneracies at the beginning and the end of the time evolution, complicating the transfer process.

IV. AQT CASCADE

The AQT process described above transfers qubit states between three electrons. We now show that AQT processes can be cascaded to enable long-distance state transfer. We use two AQT steps in a chain of four qubits [Fig. 4(a)]. We initialize the qubit chain in the state $|S_{12} \downarrow_3 \uparrow_4\rangle$ (or $|S_{12} \uparrow_3 \downarrow_4\rangle$). In the first AQT, we set $[J_1(t), J_2(t), J_3(t)] = J^{max}[1-t/T, t/T, 0]$ for $0 < t < T$, where $J^{max} = 120$ MHz and T ranges from 0 to 127 ns [Fig. 4(b)]. In the adiabatic limit, the spin state from qubit 3 transfers to qubit 1, and the singlet state in qubits 1-2 transfers to qubits 2-3 so that the spin state

of the qubit chain becomes $|\downarrow_1 S_{23} \uparrow_4\rangle$ (or $|\uparrow_1 S_{23} \downarrow_4\rangle$). In the second AQT step, we set $[J_1(t), J_2(t), J_3(t)] = J^{max}[0, 1-t/T, t/T]$ for $0 < t < T$. In the adiabatic limit, this process transfers the spin state of qubit 4 to qubit 2, and the singlet state in qubits 2-3 transfers to qubits 3-4 so that the final spin state of the qubit chain becomes $|\downarrow_1 \downarrow_2 S_{34}\rangle$ (or $|\uparrow_1 \downarrow_2 S_{34}\rangle$). We measure the left and right pairs as before.

Figures 4(c)-(d) show the cases for $f = +1$ and -1 , respectively. Even though the data of Figs. 4(c)-(d) involve two AQT steps, the maximum transfer probability appears higher than the data of Figs. 3(c)-(d), which involve one AQT step and two SWAP gates. We attribute this difference to the relative insensitivity of the AQT process to noise and pulse errors, as compared to the SWAP gates. This difference highlights the robustness and potential usefulness of AQT in quantum-dot spin chains. As before, our simulations agree with our measurements.

To verify successful transfer via cascaded AQT steps, we induce exchange between qubits 1-2 and singlet-triplet evolution between qubits 3-4 following the state transfer [33]. The data from these measurements are shown in the insets of Figs. 4(c)-(d). The presence of coherent oscillations in both cases confirms successful transfer of single-spin eigenstates and two-spin entangled states.

As in Figs. 3(c)-(d), the data of Figs. 4(c)-(d) show oscillatory features at small values of T , which are related to resonant adiabatic quantum transfer [23]. These resonances in the non-adiabatic limit provide a shortcut to adiabatic quantum-state transfer. In the present experiment, effects associated with the hyperfine gradient broaden and reduce the overall fidelity of the resonant peaks. We expect that resonant adiabatic transfer should work better in Si spin qubits, where nuclear spin effects

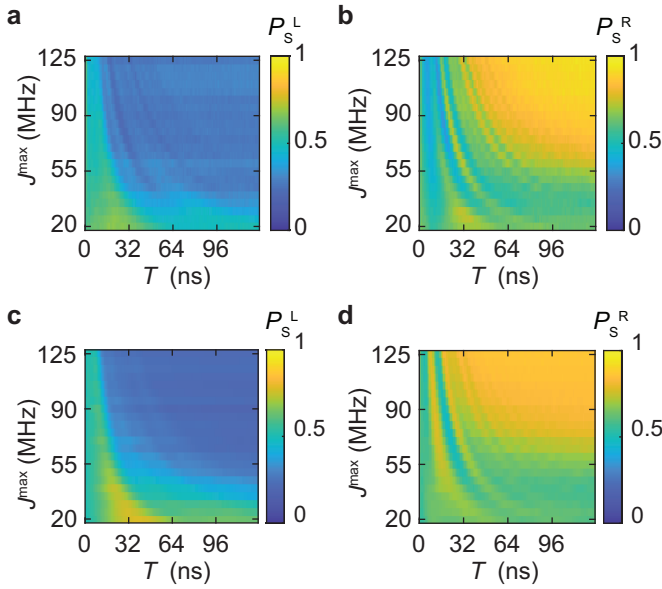


FIG. 5. Effects of maximum coupling strength J^{max} and interpolation time T . (a) Singlet return probability of the left pair, and (b) the right pair as a function of J^{max} and T . (c-d) Simulations corresponding to (a) and (b), respectively. During this experiment, we observed that in most cases $f = -1$. Therefore, we did not post-select the data in these panels [33].

are suppressed.

To further explore effects associated with the speed of the state transfer, we plot measurements of the cascaded AQT probability as we vary T and J^{max} (Fig. 5). We find that increasing J^{max} or T both correlate with higher transfer fidelity. This is expected, because the condition for adiabatic transfer is $J^{max}T/\hbar \gg 1$ [23]. We also observe prominent features associated with resonant adiabatic transfer, especially at low values of T . Although harnessing resonant adiabatic transfer requires more precise control pulses than adiabatic transfer, it provides a route to distant state transfer in shorter times than adiabatic transfer.

V. DISCUSSION

Our experiments show that AQT is a promising tool for quantum state transfer in semiconductor quantum-dot spin chains. Unlike methods for state transfer based on shuttling, AQT involves transferring quantum states without moving the qubits themselves, simplifying the process.

The presence of a magnetic field gradient limits the fidelity of AQT by limiting the fidelity of the singlet preparation. The details of the magnetic gradient also determine the precise eigenenergies of the system. In general, a magnetic gradient will tend to decrease the energy gaps in the system, requiring a slower pulse and lowering the overall transfer fidelity [33].

Magnetic fluctuations also tend to lower the fidelity.

The fidelity of AQT with $J^{max} = 120$ MHz, assuming perfect state preparation and measurement, but including pulse imperfections, hyperfine noise, and charge noise, is estimated to be > 0.95 for both spin eigenstates and the singlet state [33]. For arbitrary single-qubit states, we simulate that the AQT fidelity is about 0.7 in the present device. In Si spin qubits, where nuclear spin noise is suppressed, we expect that AQT can enable high-fidelity transfer of arbitrary states [23, 33]. For example, when $T_2^* > 1 \mu\text{s}$ for single-spins, as is the case in isotopically purified Si, we simulate that transfer fidelities can exceed 0.99 for arbitrary single-qubit states. Encouragingly, the essential elements of the AQT process, including barrier-controlled exchange coupling [39, 43] and Pauli spin-blockade readout [44, 45] are now common in Si spin qubits.

Our current method of exchange-coupling control lets us set the couplings with an accuracy of about 10 MHz [10]. Although we intend to ramp the exchange couplings linearly, errors in our exchange-coupling calibration can cause slight deviations from a linear ramp. These deviations can reduce the overall fidelity, especially if the couplings are ramped more quickly than intended. In the future, more accurate modeling and control of exchange couplings should enable higher fidelity state transfer.

To conclude, we have demonstrated adiabatic quantum-state transfer of both single-spin eigenstates and two-spin entangled states. We have also showed that the AQT protocol can be cascaded for efficient and robust quantum information transfer in a chain of semiconductor quantum-dot spin qubits. We believe that AQT will enable quantum state transfer in long chains of spin qubits for initialization, operation, and measurement in gate-based quantum computing architectures. An exciting prospect for future work is to harness many-body entangled states for direct, long-distance AQT [27, 28]. This work also opens up the possibility of adiabatic single qubit state- and gate-teleportation, as well as universal adiabatic quantum computing, in semiconductor quantum-dot spin qubits.

VI. ACKNOWLEDGMENTS

This work was sponsored by the Defense Advanced Research Projects Agency under Grant No. D18AC00025; the Army Research Office under Grant Nos. W911NF-16-1-0260 and W911NF-19-1-0167; and the National Science Foundation under Grant DMR-1809343. The views and conclusions contained in this document are those of the authors and should not be interpreted as representing the official policies, either expressed or implied, of the Army Research Office or the U.S. Government. The U.S. Government is authorized to reproduce and distribute reprints for Government purposes notwithstanding any copyright notation herein.

[1] D. M. Zajac, T. M. Hazard, X. Mi, E. Nielsen, and J. R. Petta, "Scalable gate architecture for a one-dimensional array of semiconductor spin qubits," *Phys. Rev. Applied* **6**, 054013 (2016).

[2] C. Volk, A. M. J. Zwerver, U. Mukhopadhyay, P. T. Eendebak, C. J. van Diepen, J. P. Dehollain, T. Hensgens, T. Fujita, C. Reichl, W. Wegscheider, and L. M. K. Vandersypen, "Loading a quantum-dot based "qubyte" register," *npj Quantum Information* **5**, 29 (2019).

[3] Timothy Alexander Baart, Mohammad Shafiei, Takafumi Fujita, Christian Reichl, Werner Wegscheider, and Lieven Mark Koenraad Vandersypen, "Single-spin ccd," *Nature nanotechnology* **11**, 330 (2016).

[4] A. R. Mills, D. M. Zajac, M. J. Gullans, F. J. Schupp, T. M. Hazard, and J. R. Petta, "Shuttling a single charge across a one-dimensional array of silicon quantum dots," *Nature Communications* **10**, 1063 (2019).

[5] T. Hensgens, T. Fujita, L. Janssen, Xiao Li, C. J. Van Diepen, C. Reichl, W. Wegscheider, S. Das Sarma, and L. M. K. Vandersypen, "Quantum simulation of a fermi-hubbard model using a semiconductor quantum dot array," *Nature* **548**, 70–73 (2017).

[6] C. J. van Diepen, P. T. Eendebak, B. T. Buijtendorp, U. Mukhopadhyay, T. Fujita, C. Reichl, W. Wegscheider, and L. M. K. Vandersypen, "Automated tuning of inter-dot tunnel coupling in double quantum dots," *Applied Physics Letters* **113**, 033101 (2018).

[7] A. R. Mills, M. M. Feldman, C. Monical, P. J. Lewis, K. W. Larson, A. M. Mounce, and J. R. Petta, "Computer-automated tuning procedures for semiconductor quantum dot arrays," *Applied Physics Letters* **115**, 113501 (2019).

[8] T. K. Hsiao, C. J. van Diepen, U. Mukhopadhyay, C. Reichl, W. Wegscheider, and L. M. K. Vandersypen, "Efficient orthogonal control of tunnel couplings in a quantum dot array," (2020), arXiv:2001.07671.

[9] Justyna P Zwolak, Thomas McJunkin, Sandesh S Kalantre, JP Dodson, ER MacQuarrie, DE Savage, MG Lagally, SN Coppersmith, Mark A Eriksson, and Jacob M Taylor, "Autotuning of double-dot devices in situ with machine learning," *Physical Review Applied* **13**, 034075 (2020).

[10] Haifeng Qiao, Yadav P. Kandel, Kuangyin Deng, Saeed Fallahi, Geoffrey C. Gardner, Michael J. Manfra, Edwin Barnes, and John M. Nichol, "Coherent multi-spin exchange in a quantum-dot spin chain," (2020), arXiv:2001.02277.

[11] Yadav P. Kandel, Haifeng Qiao, Saeed Fallahi, Geoffrey C. Gardner, Michael J. Manfra, and John M. Nichol, "Coherent spin-state transfer via heisenberg exchange," *Nature* **573**, 553–557 (2019).

[12] Haifeng Qiao, Yadav P Kandel, Sreenath K Manikandan, Andrew N Jordan, Saeed Fallahi, Geoffrey C Gardner, Michael J Manfra, and John M Nichol, "Conditional teleportation of quantum-dot spin states," *Nature Communications* **11**, 1–9 (2020).

[13] Takafumi Fujita, Timothy Alexander Baart, Christian Reichl, Werner Wegscheider, and Lieven Mark Koenraad Vandersypen, "Coherent shuttle of electron-spin states," *npj Quantum Information* **3**, 22 (2017).

[14] H Flentje, P-A Mortemousque, R Thalineau, A Ludwig, AD Wieck, C Bäuerle, and T Meunier, "Coherent long-distance displacement of individual electron spins," *Nature communications* **8**, 1–6 (2017).

[15] Takashi Nakajima, Matthieu R. Delbecq, Tomohiro Otsuma, Shinichi Amaha, Jun Yoneda, Akito Noiri, Kenta Takeda, Giles Allison, Arne Ludwig, Andreas D. Wieck, Xuedong Hu, Franco Nori, and Seigo Tarucha, "Coherent transfer of electron spin correlations assisted by dephasing noise," *Nature Communications* **9**, 2133 (2018).

[16] Benoit Bertrand, Sylvain Hermelin, Shintaro Takada, Michihisa Yamamoto, Seigo Tarucha, Arne Ludwig, Andreas D Wieck, Christopher Bäuerle, and Tristan Meunier, "Fast spin information transfer between distant quantum dots using individual electrons," *Nature nanotechnology* **11**, 672 (2016).

[17] A. J. Sigillito, M. J. Gullans, L. F. Edge, M. Borselli, and J. R. Petta, "Coherent transfer of quantum information in a silicon double quantum dot using resonant swap gates," *npj Quantum Information* **5**, 110 (2019).

[18] Timothy Alexander Baart, Takafumi Fujita, Christian Reichl, Werner Wegscheider, and Lieven Mark Koenraad Vandersypen, "Coherent spin-exchange via a quantum mediator," *Nature Nanotechnology* **12**, 26–30 (2017).

[19] Filip K. Malinowski, Frederico Martins, Thomas B. Smith, Stephen D. Bartlett, Andrew C. Doherty, Peter D. Nissen, Saeed Fallahi, Geoffrey C. Gardner, Michael J. Manfra, Charles M. Marcus, and Ferdinand Kuemmeth, "Fast spin exchange across a multielectron mediator," *Nature Communications* **10**, 1196 (2019).

[20] Edward Farhi, Jeffrey Goldstone, Sam Gutmann, and Michael Sipser, "Quantum computation by adiabatic evolution," (2000), arXiv:quant-ph/0001106.

[21] Dave Bacon and Steven T. Flammia, "Adiabatic gate teleportation," *Phys. Rev. Lett.* **103**, 120504 (2009).

[22] Andrew D. Greentree, Jared H. Cole, A. R. Hamilton, and Lloyd C. L. Hollenberg, "Coherent electronic transfer in quantum dot systems using adiabatic passage," *Phys. Rev. B* **70**, 235317 (2004).

[23] Sangchul Oh, Yun-Pil Shim, Jianjia Fei, Mark Friesen, and Xuedong Hu, "Resonant adiabatic passage with three qubits," *Phys. Rev. A* **87**, 022332 (2013).

[24] R. Menchon-Enrich, A. Benseyn, V. Ahufinger, A. D. Greentree, Th. Busch, and J. Mompart, "Reports on Progress in Physics Spatial adiabatic passage: a review of recent progress Related content," *Rep. Prog. Phys.* **79** (2016).

[25] Yue Ban, Xi Chen, Sigmund Kohler, and Gloria Platero, "Spin entangled state transfer in quantum dot arrays: Coherent adiabatic and speed-up protocols," *Advanced Quantum Technologies* **2** (2019).

[26] David Petrosyan, Georgios M. Nikolopoulos, and P. Lambropoulos, "State transfer in static and dynamic spin chains with disorder," *Phys. Rev. A* **81**, 042307 (2010).

[27] Nicholas Chancellor and Stephan Haas, "Using the J1–J2 quantum spin chain as an adiabatic quantum data bus," *New Journal of Physics* **14**, 095025 (2012).

[28] Umer Farooq, Abolfazl Bayat, Stefano Mancini, and Sougato Bose, "Adiabatic many-body state preparation

and information transfer in quantum dot arrays," *Phys. Rev. B* **91**, 134303 (2015).

[29] Nikolay V. Vitanov, Andon A. Rangelov, Bruce W. Shore, and Klaas Bergmann, "Stimulated raman adiabatic passage in physics, chemistry, and beyond," *Rev. Mod. Phys.* **89**, 015006 (2017).

[30] K. S. Kumar, A. Vepsäläinen, S. Danilin, and G. S. Paraoanu, "Stimulated raman adiabatic passage in a three-level superconducting circuit," *Nature Communications* **7**, 10628 (2016).

[31] Chr Wunderlich, Th Hannemann, T Körber, H Häffner, Ch Roos, W Hänsel, R Blatt, and F Schmidt-Kaler, "Robust state preparation of a single trapped ion by adiabatic passage," *Journal of Modern Optics* **54**, 1541–1549 (2007).

[32] Antti Vepsäläinen, Sergey Danilin, and Gheorghe Sorin Paraoanu, "Superadiabatic population transfer in a three-level superconducting circuit," *Science Advances* **5** (2019), 10.1126/sciadv.aau5999.

[33] See Suppplemental Material for further information on experimental procedures, calculations, and simulations.

[34] M. Pioro-Ladrière, T. Obata, Y. Tokura, Y.-S. Shin, T. Kubo, K. Yoshida, T. Taniyama, and S. Tarucha, "Electrically driven single-electron spin resonance in a slanting zeeman field," *Nature Physics* **4** (2008).

[35] F. H. L. Koppens, C. Buijzer, K. J. Tielrooij, I. T. Vink, K. C. Nowack, T. Meunier, L. P. Kouwenhoven, and L. M. K. Vandersypen, "Driven coherent oscillations of a single electron spin in a quantum dot," *Nature* **442**, 766–771 (2006).

[36] Susan J. Angus, Andrew J. Ferguson, Andrew S. Dzurak, and Robert G. Clark, "Gate-defined quantum dots in intrinsic silicon," *Nano Letters* **7**, 2051–2055 (2007).

[37] C. Barthel, M. Kjærgaard, J. Medford, M. Stopa, C. M. Marcus, M. P. Hanson, and A. C. Gossard, "Fast sensing of double-dot charge arrangement and spin state with a radio-frequency sensor quantum dot," *Phys. Rev. B* **81**, 161308 (2010).

[38] S. A. Studenikin, J. Thorgrimsson, G. C. Aers, A. Kam, P. Zawadzki, Z. R. Wasilewski, A. Bogan, and A. S. Sachrajda, "Enhanced charge detection of spin qubit readout via an intermediate state," *Applied Physics Letters* **101**, 233101 (2012).

[39] M. D. Reed, B. M. Maune, R. W. Andrews, M. G. Borselli, K. Eng, M. P. Jura, A. A. Kiselev, T. D. Ladd, S. T. Merkel, I. Milosavljevic, E. J. Pritchett, M. T. Rakher, R. S. Ross, A. E. Schmitz, A. Smith, J. A. Wright, M. F. Gyure, and A. T. Hunter, "Reduced sensitivity to charge noise in semiconductor spin qubits via symmetric operation," *Phys. Rev. Lett.* **116**, 110402 (2016).

[40] Frederico Martins, Filip K. Malinowski, Peter D. Nissen, Edwin Barnes, Saeed Fallahi, Geoffrey C. Gardner, Michael J. Manfra, Charles M. Marcus, and Ferdinand Kuemmeth, "Noise suppression using symmetric exchange gates in spin qubits," *Phys. Rev. Lett.* **116**, 116801 (2016).

[41] J. R. Petta, A. C. Johnson, J. M. Taylor, E. A. Laird, A. Yacoby, M. D. Lukin, C. M. Marcus, M. P. Hanson, and A. C. Gossard, "Coherent manipulation of coupled electron spins in semiconductor quantum dots," *Science* **309**, 2180–2184 (2005).

[42] Sandra Foletti, Hendrik Bluhm, Diana Mahalu, Vladimir Umansky, and Amir Yacoby, "Universal quantum control of two-electron spin quantum bits using dynamic nuclear polarization," *Nature Physics* **5**, 903–908 (2009).

[43] K. Takeda, A. Noiri, J. Yoneda, T. Nakajima, and S. Tarucha, "Resonantly driven singlet-triplet spin qubit in silicon," *Phys. Rev. Lett.* **124**, 117701 (2020).

[44] A.M. Jones, E.J. Pritchett, E.H. Chen, T.E. Keating, R.W. Andrews, J.Z. Blumoff, L.A. De Lorenzo, K. Eng, S.D. Ha, A.A. Kiselev, S.M. Meenehan, S.T. Merkel, J.A. Wright, L.F. Edge, R.S. Ross, M.T. Rakher, M.G. Borselli, and A. Hunter, "Spin-blockade spectroscopy of Si/Si-Ge quantum dots," *Phys. Rev. Applied* **12**, 014026 (2019).

[45] Elliot J. Connors, JJ Nelson, and John M. Nichol, "Rapid high-fidelity spin-state readout in Si/Si-Ge quantum dots via rf reflectometry," *Phys. Rev. Applied* **13**, 024019 (2020).

Supplementary Material for

Adiabatic quantum state transfer in a semiconductor

quantum-dot spin chain

Yadav P. Kandel,¹ Haifeng Qiao,¹ Saeed Fallahi,^{2,3} Geoffrey C. Gardner,^{3,4} Michael J. Manfra,^{2,3,4,5} and John M. Nichol^{1,*}

¹*Department of Physics and Astronomy,*

University of Rochester, Rochester, NY, 14627 USA

²*Department of Physics and Astronomy,*

Purdue University, West Lafayette, IN, 47907 USA

³*Birck Nanotechnology Center, Purdue University, West Lafayette, IN, 47907 USA*

⁴*School of Materials Engineering, Purdue University, West Lafayette, IN, 47907 USA*

⁵*School of Electrical and Computer Engineering,*

Purdue University, West Lafayette, IN, 47907 USA

A. Device

Our four-qubit quantum processor is fabricated on a GaAs/AlGaAs semiconductor heterostructure. The two-dimensional electron gas (2DEG) resides at the interface between the GaAs and AlGaAs layers, 91 nm below the surface of the wafer. The density and mobility of carriers in the 2DEG at a temperature of 4 K are $1.5 \times 10^{11} \text{ cm}^{-2}$ and $2.5 \times 10^6 \text{ cm}^2/\text{Vs}$, respectively. Aluminum gates are arranged in a three-layer overlapping gate architecture and are fabricated using electron beam lithography. An additional top gate, not shown in Fig. 1(a) in the main text, covers all of the gates and the space around the center of device. Each of these metal gates are separated by ~ 10 nm of native oxide formed on the gate surface. Voltages applied to the gates confine the qubit-host electrons in the 2DEG. Each dot contains only one electron, and their chemical potentials are roughly the same, which we refer to as the symmetric configuration. The plunger and barrier gates are connected to arbitrary waveform generator channels via home made bias-tees. This configuration en-

* john.nichol@rochester.edu

ables fast initialization, manipulation, and readout of spin qubits. Further details about the device are given in Ref. [1].

B. Orthogonal control of the chemical potentials and exchange couplings

Our device has four plunger gates $[p_1, p_2, p_3, p_4]$ for chemical potential control, three barrier gates $[b_1, b_2, b_3]$ for controlling the tunnel coupling between adjacent dots, and leads $[L_1, L_2]$ for controlling the system-environment interaction. In order to achieve individual control over the chemical potentials and exchange couplings, we define a set of virtual gates $\mathbf{G} = [P_1, P_2, P_3, P_4, B_1, B_2, B_3]^T$ as $\mathbf{G} = A \cdot \mathbf{g}$, where $\mathbf{g} = [p_1, p_2, p_3, p_4, b_1, b_2, b_3]^T$ is a set of physical gates, and A is a 7×7 capacitance matrix [2–4]. We achieve orthogonal control of the exchange couplings $\mathbf{J} = [J_1, J_2, J_3]$ by defining it as a non-linear function of the “virtual” barrier gates using the Heitler-London model [4, 5]. Schematics of the virtual-gate pulses used to implement the AQT circuits shown in Figs. 3(a) and 4(a) in the main text are shown in Supplementary Figs. 1(a) and (b), respectively.

C. State preparation and readout

For initialization and readout, we configure the quadruple quantum-dot chain into two pairs. Dots 1 and 2 form the “left” pair and dots 3 and 4 form the “right” pair. We initialize the system in the $(2, 0, 0, 2)$ charge state by lowering the chemical potentials of dots 1 and 4 below the Fermi level of the corresponding reservoir, while holding the chemical potentials of dots 2 and 3 above the Fermi level of that reservoir. The ground state of a pair of electrons in a single dot is the singlet state. We transfer one electron each from dots 1 and 4 into dots 2 and 3, respectively. Diabatic charge transfer maintains the joint spin states of the electrons, while adiabatic charge transfer prepares the electrons in spin eigenstates. We can also initialize either pair in the $|\uparrow\uparrow\rangle$ state. Measurement via Pauli spin blockade and safeguards to eliminate cross-talk are detailed in Refs. [1, 4].

The experimental data of Figs. 3 and 4 in the main text involve measuring a singlet in the right pair. Generally, diabatic charge transfer together with a Pauli spin-blockade measurement suffice to measure a pair of electrons in the singlet-triplet basis [6, 7]. However, the small inter-dot tunnel coupling limits the fidelity of diabatic projection in our device.

To measure a pair of electrons in the singlet-triplet basis in our device, we implemented a modified pulse sequence in which the electron pair is first evolved under the two-electron Hamiltonian

$$H_{i,i+1}^{\text{read}} = J_i^{\text{max}}(1-t/\tau) \frac{\hbar}{4} \boldsymbol{\sigma}_i \cdot \boldsymbol{\sigma}_{i+1} + \frac{\hbar}{2} (B_i^z \sigma_i^z + B_{i+1}^z \sigma_{i+1}^z), \quad (1)$$

where τ is the evolution time, and J_i^{max} is the exchange coupling. To implement this Hamiltonian, we suddenly turn on a large exchange coupling between the two electrons, and slowly ramp it to zero. This procedure maps the singlet state to $|\uparrow\downarrow\rangle$ (or $|\downarrow\uparrow\rangle$, depending on the sign of the hyperfine gradient). Then we readout the electron pair by adiabatic projection, which remaps the state to the singlet-triplet basis. Typical values used in the experiment are $\tau = 2 \mu\text{s}$ and $J_i^{\text{max}} = 300 \text{ MHz}$. A related method can be used to prepare entangled states in quantum-dot arrays [8]. This method can also be used to implement a true counterintuitive pulse sequence (Supplementary Fig. 6) [9, 10].

D. Ground state of the magnetic field gradient

To prepare the spin chain in a product state with $S^z = 0$, we load two electrons in dots 1 and 4 each and transfer one electron from each of them to dots 2 and 3 adiabatically. The particular orientation of the spins in the chain after this step depends on the ground state of the hyperfine field gradient on both sides [6, 7]. Since the hyperfine field fluctuates in time, the gradient also changes, and so does the ground-state spin configuration. Because our experiments involve preparing spin states on one side of the array and transferring them to the other side before the measurement, knowledge of the hyperfine configuration is critical. As we now discuss, we can monitor not only the sign of the gradients but also the ground-state spin configurations of the left and right sides in real time by measuring the evolution of the spin states in dots 2-3 under exchange coupling.

We define $f = \text{sign}(B_2^z - B_1^z) \times \text{sign}(B_4^z - B_3^z)$. In order to measure f , we initialize both sides as a product state with $S^z = 0$, which we denote as the SS configuration. We then evolve electrons 2 and 3 under exchange coupling for variable amount of time. When $f = +1$, the initial state of the chain is $|\uparrow_1\downarrow_2\uparrow_3\downarrow_4\rangle$ or $|\downarrow_1\uparrow_2\downarrow_3\uparrow_4\rangle$. In these cases, the orientations of spins 2 and 3 are opposite, and they oscillate under exchange coupling. Adiabatic projection of the left and right sides, followed by measurement in the singlet/triplet basis, yields prominent exchange oscillations. But for $f = -1$, the initial state of the chain is $|\uparrow_1\downarrow_2\downarrow_3\uparrow_4\rangle$ or $|\downarrow_1\uparrow_2\uparrow_3\downarrow_4\rangle$.

In these cases, the orientations of spins 2 and 3 are the same, and no exchange oscillations occur.

To determine the ground-state spin orientation, we load the left side in the $|\uparrow\uparrow\rangle$ state and the right side in a product state with $S^z = 0$. We denote this as the T^+S configuration, and we turn on exchange coupling between spins 2 and 3. For $\Delta B_{34}^z > 0$, the spin state after initialization is $|\uparrow_1\uparrow_2\downarrow_3\uparrow_4\rangle$, and exchange oscillations between spins 2 and 3 can occur. However for $\Delta B_{34}^z < 0$, the the spin configuration of the chain after loading is $|\uparrow_1\uparrow_2\uparrow_3\downarrow_4\rangle$ and the spin states of electrons 2-3 do not evolve under exchange. The ground state spin-configuration in dots 1-2 can be inferred from the combined knowledge of f and the spin configuration in dots 3-4. Supplementary Fig. 2 illustrates these measurements.

E. Post-selection of data

The ground-state spin orientation of the qubit chain was monitored during experiments by interleaving the pulses discussed above. Specifically, we interleaved measurements of exchange between qubits 2 and 3 with the SS and T^+S configurations (Supplementary Fig. 2). When qubits 2-3 oscillate under exchange coupling with the SS load, the ideal time-averaged singlet return probability on the right/left side is $\left[P_S^{R/L}\right]_t = 0.5$ for $f = +1$. When $f = -1$ and the qubits do not oscillate, $\left[P_S^{R/L}\right]_t = 1$. The measured values of $\left[P_S^{R/L}\right]_t$ may deviate from the ideal expectation due to a large ΔB_{23}^z , load errors, or measurement errors. Thus, we define a threshold on the time averaged singlet return probability as $P_{th} = 0.75$, which is the mean of the two ideal values. We assume $f = +1$ when $\left[P_S^{R/L}\right]_t < P_{th}$ and $f = -1$ when $\left[P_S^{R/L}\right]_t > P_{th}$.

The data associated with Figs. 3 and 4 in the main text consist of many repetitions. Each repetition, which consists of 512 and 256 single-shot measurements for Figs. 3 and 4 respectively corresponding to each value of T , was assigned a value of f based on the interleaved measurement discussed above. Individual repetitions with different values of f are displayed in the main text. The data from all repetitions of the AQT experiments, as well as the average of the $f = \pm 1$ cases corresponding to Figs. 3, 4, and 5 of the main text are shown in Supplementary Figs. 3, 4, and 5, respectively. The averages across all $f = \pm 1$ cases do not differ substantially from the individual repetitions displayed in the main text.

F. Counterintuitive AQT process

In the main text, we described an AQT protocol where two out of the three qubits involved in the process began as a singlet. However, we can also implement AQT in a chain of electron-spin eigenstates by using a “counterintuitive” pulse sequence [Supplementary Fig. 6(a)] [9, 10]. For this, we initialized both sides in the ground state of the magnetic field gradient with $S^z = 0$. In order to transfer the spin state of qubit 2 to qubit 4, we first turned on the exchange coupling between qubits 3 and 4. For this, we evolved the qubit-chain under the Hamiltonian

$$H_0(t) = J^{max} \frac{t}{\tau} \frac{\hbar}{4} \boldsymbol{\sigma}_3 \cdot \boldsymbol{\sigma}_4 + \frac{\hbar}{2} \sum_{i=1}^4 B_i^z \sigma_i^z, \quad (2)$$

where $J^{max} = 300$ MHz, and $\tau = 2$ μ s is the ramp time. Then the qubit chain is evolved under the Hamiltonian

$$H_{jkl}(t) = J^{max} \frac{\hbar}{4} \left[\frac{t}{T} \boldsymbol{\sigma}_j \cdot \boldsymbol{\sigma}_k + \left(1 - \frac{t}{T}\right) \boldsymbol{\sigma}_k \cdot \boldsymbol{\sigma}_l \right] + \frac{\hbar}{2} \sum_{i=1}^4 B_i^z \sigma_i^z, \quad (3)$$

with $(j, k, l) = (2, 3, 4)$, where $J^{max} = 120$ MHz. In the adiabatic limit, this process transfers the spin state of qubit 2 to qubit 4. Next, we transferred the state of qubit 1 to qubit 3 by turning off the exchange coupling between qubits 2 and 3 and turning on the coupling between qubits 1 and 2, as described by the Hamiltonian in Eq. (3) with $(j, k, l) = (1, 2, 3)$. Finally, we turned off the exchange coupling between qubits 1 and 2, as described by the Hamiltonian in Eq. (1), and we measured both sides by adiabatic projection onto the singlet/triplet basis. The spin ground states were monitored during this experiment as described above. The circuit diagram for this experiment, and the post-selected data are shown in Supplementary Figs. 6(a-e).

G. Indirect AQT fidelity assessment

As an indirect qualitative indicator of the AQT fidelity, we transferred states of the qubit chain initialized in the state $|S_{12}\uparrow_3\downarrow_4\rangle$ or $|S_{12}\downarrow_3\uparrow_4\rangle$ via a cascade of AQT steps, with $T = 127$ ns and varying J^{max} . Then, we evolved qubits 1-2 and qubits 3-4 under exchange coupling for a variable amount of time [Supplementary Fig. 5(f)]. The measured singlet return probabilities on both sides were fitted to a function of the form $P_S^{R/L}(t) = V^{R/L} \cos(2\pi J_i t + \phi) \exp(-t^2/T_2^{*2}) + P_0$, where $V^{R/L}$ is the visibility of exchange oscillations

on the right/left side, J_i is the frequency of exchange oscillations where $i = 1$ for the left side and $i = 3$ for the right side, t is the evolution time, ϕ is a phase factor, T_2^* is the dephasing time, and P_0 is the average of the time series. Here, $V^{R/L}$, J_i , ϕ , T_2^* , and P_0 are fit parameters. In the adiabatic limit, qubits 1 and 2 should be in a product state, and qubits 3 and 4 should be in a singlet state at the end of the cascaded AQT sequence. As seen in Supplementary Fig. 5(g), $V^{L(R)}$ increases (decreases) in J^{max} and finally saturates, as expected for adiabatic state transfer. For small values of J^{max} , V^L is small due to the low AQT fidelity, and V^R is relatively large due to dephasing of the singlet on the left side because of the hyperfine noise. Apart from the infidelity of the AQT, the visibilities are limited by load and measurement errors, hyperfine noise, and charge noise.

H. Simulation

We accounted for known sources of errors and noise to reproduce experimental observations in the simulations. Load errors associated with the singlet, and the hyperfine ground state with $S^z = 0$ were approximated by

$$\begin{aligned} |\tilde{S}\rangle &= s_1 |S\rangle + s_2 |T^0\rangle + s_3 |T^+\rangle + s_4 |T^-\rangle \\ |\tilde{G}\rangle &= s_1 |\uparrow\downarrow\rangle + s_2 |\downarrow\uparrow\rangle + s_3 |T^+\rangle + s_4 |T^-\rangle \end{aligned} \quad (4)$$

where $|S\rangle = (|\uparrow\downarrow\rangle - |\downarrow\uparrow\rangle)/\sqrt{2}$, $|T^0\rangle = (|\uparrow\downarrow\rangle + |\downarrow\uparrow\rangle)/\sqrt{2}$, $|T^+\rangle = |\uparrow\uparrow\rangle$, and $|T^-\rangle = |\downarrow\downarrow\rangle$. s_i is the probability amplitude of loading corresponding two-electron state. $f_S = |s_1|^2$, and $|s_2|^2 = |s_3|^2 = |s_4|^2 = \frac{1-f_S}{3}$, where f_S is singlet load fidelity. Based on measurements of the load process, we estimate that $f_s = 0.95$.

We define time dependent Hamiltonians acting on the qubit chain

$$\begin{aligned} H_1(t) &= J^{max} \frac{\hbar}{4} \left[\left(1 - \frac{t}{T}\right) \boldsymbol{\sigma}_1 \cdot \boldsymbol{\sigma}_2 + \frac{t}{T} \boldsymbol{\sigma}_2 \cdot \boldsymbol{\sigma}_3 \right] + \frac{\hbar}{2} \sum_{i=1}^4 B_i^z \sigma_i^z, \\ H_2(t) &= J^{max} \frac{\hbar}{4} \left[\left(1 - \frac{t}{T}\right) \boldsymbol{\sigma}_2 \cdot \boldsymbol{\sigma}_3 + \frac{t}{T} \boldsymbol{\sigma}_3 \cdot \boldsymbol{\sigma}_4 \right] + \frac{\hbar}{2} \sum_{i=1}^4 B_i^z \sigma_i^z. \end{aligned} \quad (5)$$

To simulate the AQT and SWAP experiment described in Fig. 3 in the main text, the qubit chain was initialized in the state $|\psi_0\rangle = |\tilde{S}\rangle \otimes |\tilde{G}\rangle$. The state of the qubit chain after the AQT, $|\psi_T\rangle$, was obtained by numerical integration of the time-dependent Schrodinger equation:

$$|\psi_T\rangle = U_B \prod_{j=0}^N \exp(-iH_1(j\Delta t)\Delta t/\hbar) U_B |\psi_0\rangle,$$

where $N \times \Delta t = T$ and we used $\Delta t = 1$ ns for all simulations. Here, $U_B = \exp(-i\pi \sum_{j=1}^4 B_j^z \sigma_j^z t_{wait})$ is the evolution operator corresponding to the rise and fall time of the barrier pulses [11]. We used $t_{wait} = 1$ ns in all simulations. The SWAP operation between qubit pair j and $j+1$ was generated by a unitary operator $U_{j(j+1)} = \exp(-iH_{j(j+1)}^S T_S/\hbar)$, where T_S is the π -pulse time, and $H_{j(j+1)}^S$ is

$$H_{j(j+1)}^S = J_j \frac{\hbar}{4} \boldsymbol{\sigma}_j \cdot \boldsymbol{\sigma}_{j+1} + \frac{\hbar}{2} \sum_{j=1}^4 B_j^z \sigma_j^z. \quad (6)$$

The final state of the qubit chain after the AQT and SWAP operations U_{34} and U_{23} is $|\psi_f\rangle = U_B U_{23} U_{34} |\psi_T\rangle$.

Similarly, for the simulation of the cascaded AQT experiment described in Fig. 4 of the main text, the initial state was set as $|\psi_0\rangle = |\tilde{S}\rangle \otimes |\tilde{G}\rangle$. The state of the qubits after the AQT cascade was obtained by evaluating

$$|\psi_f\rangle = U_B \prod_{k=0}^N \exp(-iH_2(k\Delta t)\Delta t/\hbar) \left(\prod_{j=0}^N \exp(-iH_1(j\Delta t)\Delta t/\hbar) U_B |\psi_0\rangle \right),$$

where $N \times \Delta t = T$. The values of T and J^{max} were set to be the same as in the corresponding experiments. The target states for both experiments are $|\varphi^R\rangle = |S\rangle$, and

$$|\varphi^L\rangle = \begin{cases} |\uparrow\downarrow\rangle, & \text{for } \Delta B_{34}^z < 0 \\ |\downarrow\uparrow\rangle, & \text{for } \Delta B_{34}^z > 0. \end{cases} \quad (7)$$

Finally, the singlet return probabilities were calculated as $P_S^{L/R} = |\langle \varphi^{L/R} | \psi_f \rangle|^2$.

The magnetic field in all simulations incorporates both the externally applied magnetic field of 0.5 Tesla and the local hyperfine field. The values of the hyperfine field and its fluctuations were adjusted for better agreement between the simulation and the experimental data, and the specific values are presented in Supplementary Table I. Charge noise directly affects the strength of exchange couplings. Noise in the exchange couplings was incorporated by sampling it from a Gaussian distribution with a target mean value (J_0) and standard deviation equal to $J_0/(\sqrt{2}\pi Q)$. The exchange oscillation quality factors Q for qubit pairs 1-2, 2-3, and 3-4 are ~ 15 , ~ 15 , and ~ 20 , respectively. The simulated data were averaged over 256 realizations of noise and errors.

To include errors due to relaxation during the measurement, we define $g = 1 - \exp(-t_m/T_1)$ where t_m is measurement time and T_1 is relaxation time. g is the probability that the excited state will relax to the ground state during readout. We define $1 - f_r$ as the probability to

Figure in the main text	Hyperfine field (MHz)	Hyperfine field noise (MHz)
3(c)	[7.90, -4.30, 51.40, -25.60]	[0.10, 0.10, 0.10, 0.10]
3(d)	[36.70, 10.10, -20.10, 7.40]	[0.10, 0.10, 0.10, 0.10]
4(c)	[-17.54, -16.12, -1.84, 31.92]	[0.10, 0.10, 0.10, 0.10]
4(d)	[-10.52, -17.55, 3.65, 24.11]	[0.10, 0.10, 0.10, 0.10]
5(c)-(d)	[20.00, 5.00, 25.00, 75.00]	[10.00, 10.00, 10.00, 10.00]

Supplementary Table I. Specific values of the hyperfine field and noise at each dot location used in different simulations.

misidentify the joint spin state due to noise. The simulated return probability including relaxation and readout errors for either side is

$$\tilde{P}_S^{R/L} = (2f_r - g - 1)P_S^{R/L} + g - f_r + 1. \quad (8)$$

Specific values of t_m , T_1 , and f_r used in the simulations are 4 μ s, 60 μ s, and 0.99 for the left side, and 6 μ s, 50 μ s, and 0.95 for the right side, respectively.

I. State-transfer fidelity estimation

In order to calculate the state transfer fidelity excluding the effects of state preparation and readout errors, we simulated a three qubit system in the state $|S_{12}\phi_3\rangle$, where $|\phi\rangle$ is a single qubit state. We evolved this state in time under the Hamiltonian $H_1(t)$ defined in Eq. (5). We estimated the single-spin transfer fidelity of the AQT process as the probability of finding qubit 1 in the $|\phi\rangle$ state after the adiabatic evolution described above. The singlet state transfer fidelity was calculated as the probability of finding qubits 2-3 in the singlet state. We repeated this calculation for different values of the magnetic field gradient between the qubits. The results are plotted in Supplementary Figs. 7(a)-(b) for the case when $|\phi\rangle = |\uparrow\rangle$. These calculations, which neglect hyperfine and charge noise, and assume perfect pulses, suggest that one of the main limiting factors in the AQT fidelity is the presence of the magnetic field gradient. To assess the effects of hyperfine noise, in Supplementary Fig. 8, we show the simulated fidelity for arbitrary singlet-qubit states vs. single-spin T_2^* values. These simulations include charge noise and pulse imperfections. Supplementary Fig. 8 shows that for isotopically purified Si spin qubits, where $T_2^* > 1 \mu$ s, the AQT fidelity for arbitrary

single-qubit states is predicted to exceed 0.99.

[1] Yadav P. Kandel, Haifeng Qiao, Saeed Fallahi, Geoffrey C. Gardner, Michael J. Manfra, and John M. Nichol, “Coherent spin-state transfer via heisenberg exchange,” *Nature* **573**, 553–557 (2019).

[2] C. J. van Diepen, P. T. Eendebak, B. T. Buijtendorp, U. Mukhopadhyay, T. Fujita, C. Reichl, W. Wegscheider, and L. M. K. Vandersypen, “Automated tuning of inter-dot tunnel coupling in double quantum dots,” *Applied Physics Letters* **113**, 033101 (2018).

[3] A. R. Mills, M. M. Feldman, C. Monical, P. J. Lewis, K. W. Larson, A. M. Mounce, and J. R. Petta, “Computer-automated tuning procedures for semiconductor quantum dot arrays,” *Applied Physics Letters* **115**, 113501 (2019).

[4] Haifeng Qiao, Yadav P. Kandel, Kuangyin Deng, Saeed Fallahi, Geoffrey C. Gardner, Michael J. Manfra, Edwin Barnes, and John M. Nichol, “Coherent multi-spin exchange in a quantum-dot spin chain,” (2020), arXiv:2001.02277.

[5] Rogerio de Sousa, Xuedong Hu, and S. Das Sarma, “Effect of an inhomogeneous external magnetic field on a quantum-dot quantum computer,” *Phys. Rev. A* **64**, 042307 (2001).

[6] J. R. Petta, A. C. Johnson, J. M. Taylor, E. A. Laird, A. Yacoby, M. D. Lukin, C. M. Marcus, M. P. Hanson, and A. C. Gossard, “Coherent manipulation of coupled electron spins in semiconductor quantum dots,” *Science* **309**, 2180–2184 (2005).

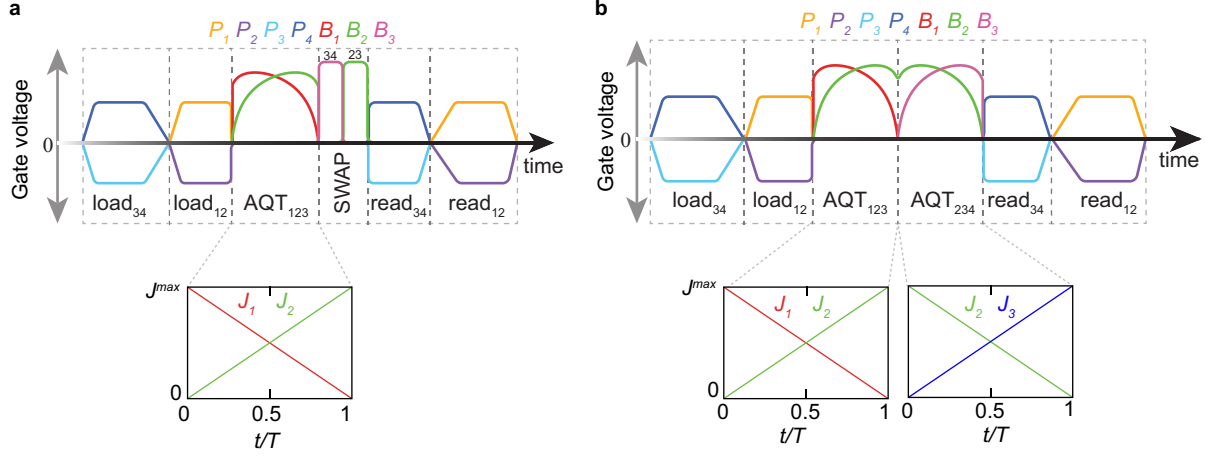
[7] Sandra Foletti, Hendrik Bluhm, Diana Mahalu, Vladimir Umansky, and Amir Yacoby, “Universal quantum control of two-electron spin quantum bits using dynamic nuclear polarization,” *Nature Physics* **5**, 903–908 (2009).

[8] Umer Farooq, Abolfazl Bayat, Stefano Mancini, and Sougato Bose, “Adiabatic many-body state preparation and information transfer in quantum dot arrays,” *Phys. Rev. B* **91**, 134303 (2015).

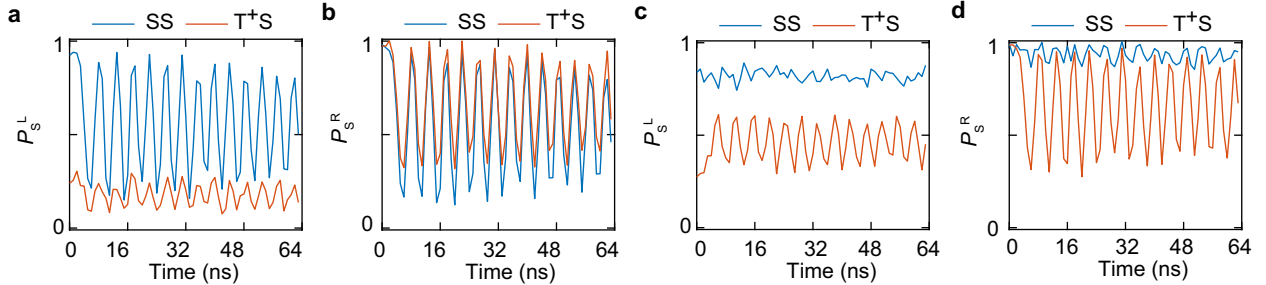
[9] Nikolay V. Vitanov, Andon A. Rangelov, Bruce W. Shore, and Klaas Bergmann, “Stimulated raman adiabatic passage in physics, chemistry, and beyond,” *Rev. Mod. Phys.* **89**, 015006 (2017).

[10] Sangchul Oh, Yun-Pil Shim, Jianjia Fei, Mark Friesen, and Xuedong Hu, “Resonant adiabatic passage with three qubits,” *Phys. Rev. A* **87**, 022332 (2013).

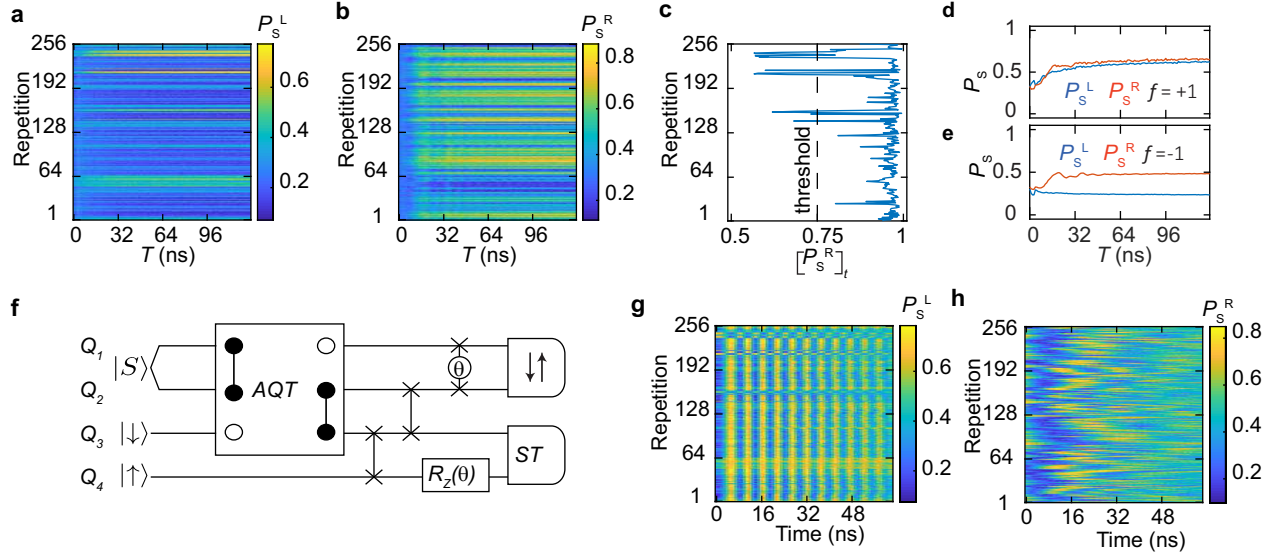
[11] Haifeng Qiao, Yadav P Kandel, Sreenath K Manikandan, Andrew N Jordan, Saeed Fallahi, Geoffrey C Gardner, Michael J Manfra, and John M Nichol, “Conditional teleportation of quantum-dot spin states,” *Nature Communications* **11**, 1–9 (2020).



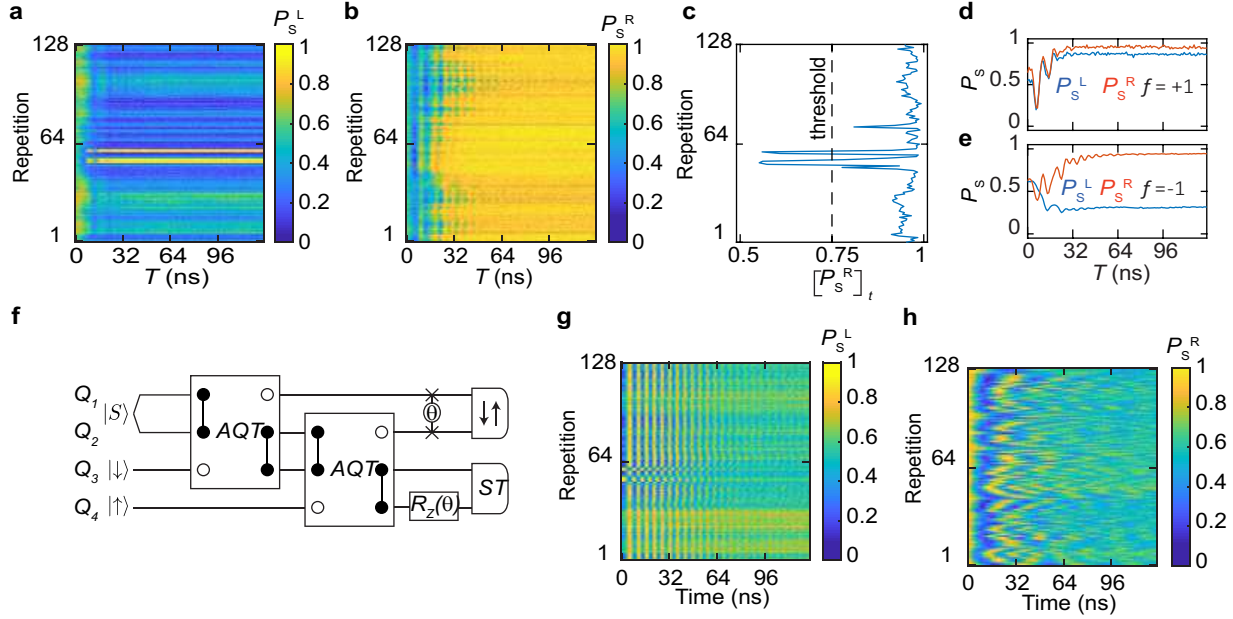
Supplementary Figure 1. Schematic of pulse diagrams for the AQT experiments. (a) Pulse timing diagram corresponding to Fig. 3(a) in the main text. (b) Pulse timing diagram corresponding to the Fig. 4(a) in the main text. Pulses for the modified method to project a two-electron state onto the singlet/triplet (*ST*) basis are omitted for clarity.



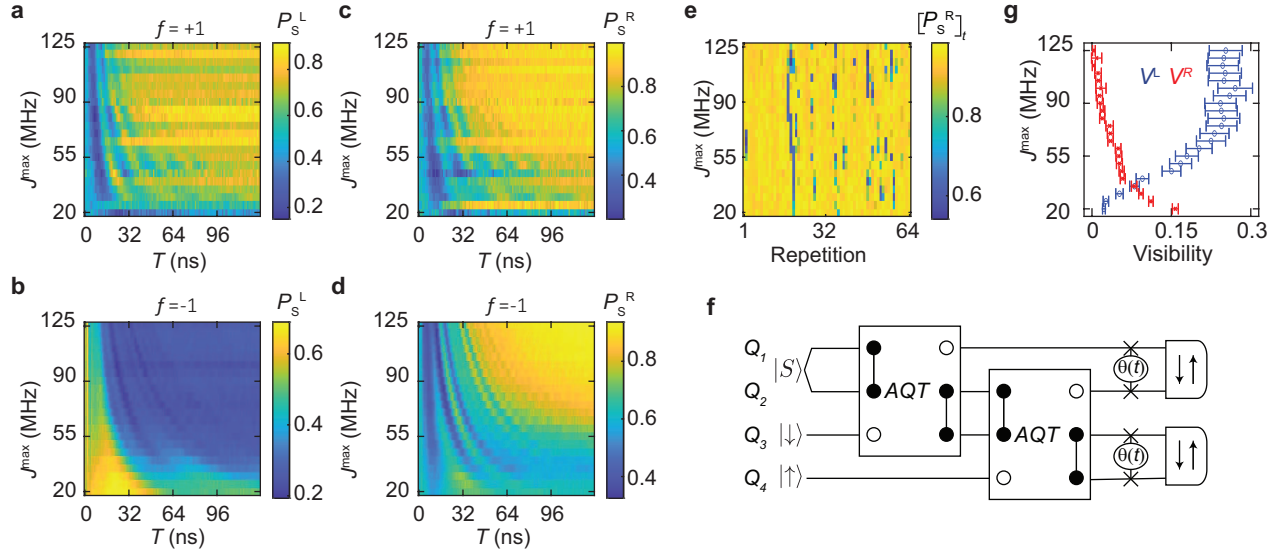
Supplementary Figure 2. Exchange oscillations of qubits 2-3 with different load conditions measured on (a, c) the left side and (b, d) the right side. The measurements of panels (a-b) were interleaved together and averaged for 256 single shot measurements. The measurements of panels (c-d) were also interleaved. In panels (a-b), prominent oscillations in the case of an *SS* initialization imply $f = +1$. Prominent oscillations in P_s^R associated with the T^+S load prove that the ground-state spin orientation in dots 3-4 is $|\downarrow\uparrow\rangle$. From this, we can also infer that the ground state spin configuration in dots 1-2 is $|\downarrow\uparrow\rangle$. Panels (c-d) show a similar data set to panels (a-b), but these data were taken at a different time with a different hyperfine configuration. The oscillations in P_s^R associated with the T^+S initialization, and the absence of oscillations associated with the *SS* initialization, imply that the ground-state spin configuration of the qubit chain is $|\uparrow\downarrow\uparrow\downarrow\rangle$, and $f = -1$.



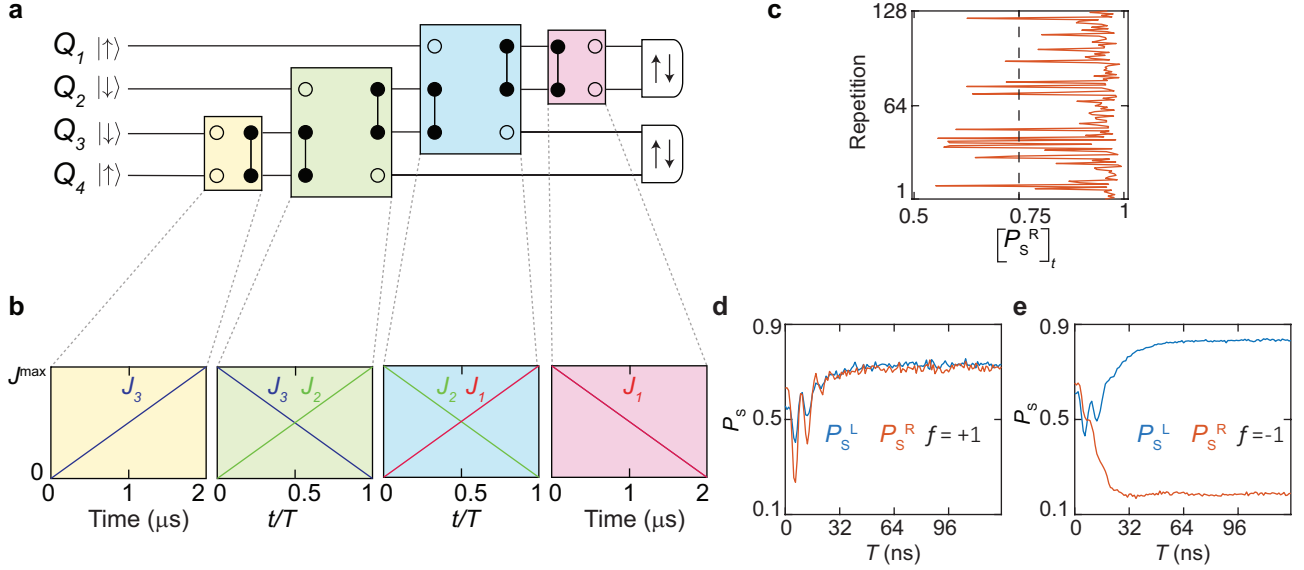
Supplementary Figure 3. (a-b) Data for all repetitions of the experiment described in Fig. 3 in the main text. The line-to-line variations are caused by hyperfine fluctuations, which affect the AQT and the SWAP gates. (c) Time-averaged right-side singlet return probabilities $[P_S^R]_t$ associated with the evolution of qubits 2-3 under the exchange coupling after *SS* initialization. These measurements were used to determine f . (d-e) Averages over all repetitions of the data in (a-b) corresponding to $f = \pm 1$. (f) Circuit diagram for the verification experiments. The spins are initialized in the state $|S_{12} \uparrow_3 \downarrow_4\rangle$ or $|S_{12} \downarrow_3 \uparrow_4\rangle$. After the AQT and SWAP operations, qubits 1-2 evolve under exchange and qubits 3 – 4 evolve under ΔB_{34}^z for variable amounts of time. (g-h) Results of the verification experiments. The exchange oscillations in (g) and the singlet-triplet oscillations in (h) prove the success of the AQT. In (g), the phase of the oscillations is opposite for $f = \pm 1$, as expected. The frequency of the singlet-triplet oscillations in (h) changes between repetitions because of the fluctuating ΔB_{34}^z . The main experiment, the verification experiment, and measurements to monitor the spin ground were interleaved in time. In panels (a), (b), (g), and (h), each line is averaged over 512 single shot measurements.



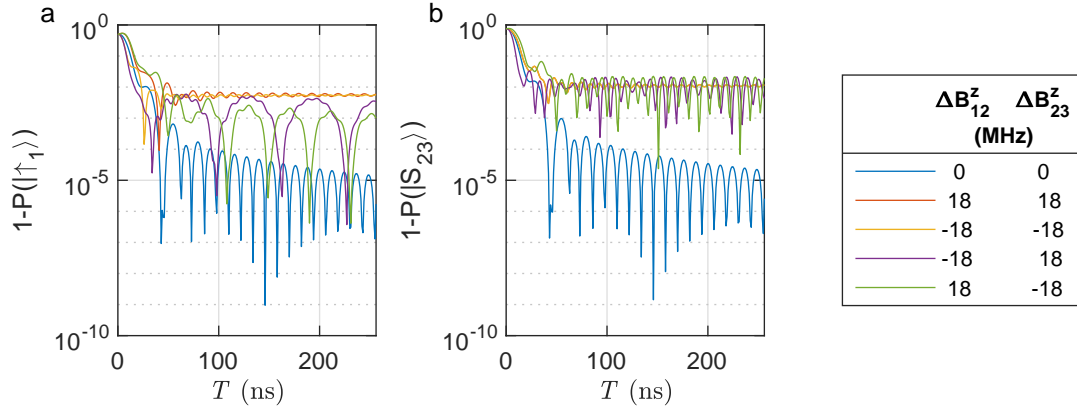
Supplementary Figure 4. (a-b) Data for all repetitions of the AQT cascade experiment described in Fig. 4 in the main text. (c) Time-averaged right-side singlet return probabilities $[P_s^R]_t$ associated with the evolution of qubits 2-3 under the exchange coupling after *SS* initialization. These measurements were used to determine f . (d-e) Averages over all repetitions of the data in (a-b) corresponding to $f = \pm 1$. (f) Circuit diagram for the verification experiments. The spins are initialized in the state $|S_{12} \uparrow_3 \downarrow_4\rangle$ or $|S_{12} \downarrow_3 \uparrow_4\rangle$. After the AQT cascade, qubits 1-2 evolve under exchange and qubits 3-4 evolve under ΔB_{34}^z for variable amounts of time. (g-h) Results of the verification experiments. The exchange oscillations in (g) and the singlet-triplet oscillations in (h) prove the success of the AQT. In (g), the phase of the oscillations is opposite for $f = \pm 1$, as expected. The frequency of the singlet-triplet oscillations in (h) changes between repetitions because of the fluctuating ΔB_{34}^z . The main experiment, the verification experiment, and measurements to monitor the spin ground were interleaved in time. In panels (a), (b), (g), and (h), each line is averaged over 256 single shot measurements.



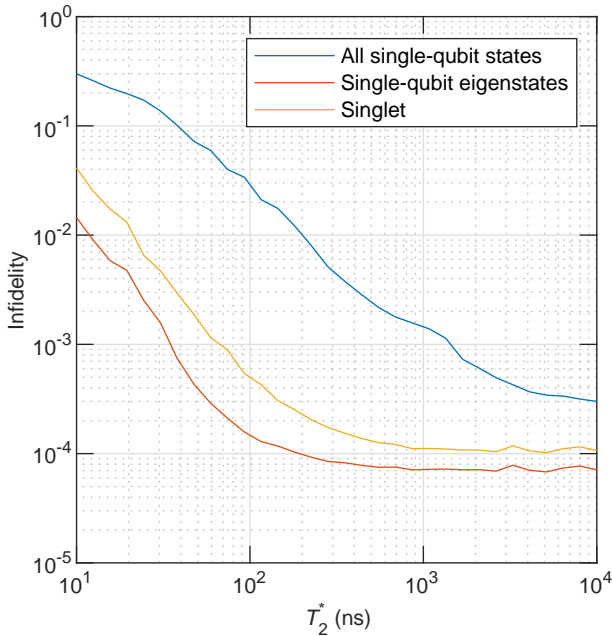
Supplementary Figure 5. Post-selection and verification data for the experiment described in Fig. 5 in the main text. (a,b) Post-selected data for the left side for $f = \pm 1$. (c,d) Post-selected data for the right side for $f = \pm 1$. (e) Time-averaged right-side singlet return probability $[P_S^R]_t$ associated with the evolution of qubits 2 and 3 under exchange coupling corresponding to SS initialization. These data indicate the value of f for the different pixels of the data represented in (a-d). We bin the main data set into $f = \pm 1$ cases by thresholding the data according to the measurements of panel (e), as discussed above. (f) Quantum circuit diagram to monitor exchange oscillation visibility after the AQT cascade. (g) Exchange oscillation visibility $V^{R/L}$ of the right and the left qubit pairs for different J^{\max} with $T = 127$ ns for $f = -1$. V^L increases gradually with J^{\max} and saturates.



Supplementary Figure 6. Adiabatic quantum-state transfer with a “counterintuitive” pulse sequence. (a) Circuit diagram of the experiment. We started with the qubit chain in a product state and implemented AQQT to transfer the spin state of qubit 2 to qubit 4 and qubit 1 to qubit 3. For the first and last steps, $J_{max} = 300$ MHz, and ramp time was set to 2 μ s. For the second and third steps, $J_{max} = 120$ MHz and T ranges from 0-127 ns. (b) The exchange coupling strengths as a function of time at different steps of the experiment. The experiment and the spin-ground-state monitoring experiments were interleaved in time. Each point the experiment was averaged for 128 single-shot measurements. (c) The time-averaged singlet return probability on the right side corresponding to evolution of qubits 2-3 under exchange coupling with *SS* initialization. Using a threshold of 0.75, we determine that 114 out of 128 repetitions correspond to $f = -1$, and 14 repetitions correspond to $f = +1$. (d-e) Average of data for all repetitions of the experiment, post-selected based on f .



Supplementary Figure 7. Simulated effects of a static magnetic field gradient on AQT fidelity. We simulated the evolution of three qubits initialized in the state $|S_{12}\uparrow_3\rangle$. We ramped down the exchange coupling between qubits 1 and 2 from 120 MHz to 0 while the exchange coupling between qubits 2 and 3 was ramped up from 0 to 120 MHz in a time T . (a) Infidelity of transferring the spin eigenstate of qubit 3 to qubit 1 as a function of T . (b) Infidelity of transferring the singlet state from qubits 1-2 to 2-3. No magnetic or charge noise was included in these simulations. The simulations show that the AQT fidelity depends sensitively on ΔB^z .



Supplementary Figure 8. Simulated error in the AQT process vs. single-spin T_2^* values. A typical T_2^* value for GaAs is 10-20 ns. For isotopically purified Si, T_2^* can exceed 1 μ s. “All single-qubit states” refers to the AQT fidelity averaged over the set of initial states $\{|+x\rangle, |-x\rangle, |+y\rangle, |-y\rangle, |+z\rangle, |-z\rangle\}$, where the letter refers to the orientation on the Bloch sphere. “Single-qubit eigenstates” refers to an average over the initial states $\{|+z\rangle, |-z\rangle\}$. “Singlet” refers to an average over all six single-qubit states of the probability of successfully transferring the singlet-state. These simulations used $J^{max} = 120$ MHz and included charge noise, as discussed above. We simulated $0 < T < 256$ ns and chose the optimal value of T for each different configuration. We averaged the simulation over 256 different noise realizations. For isotopically purified Si, these simulations suggest that the state-transfer fidelity can exceed 0.99. We hypothesize that the eventual saturation of the infidelity relates to the time-step in the simulation, which was 1 ns.